Applied Surface Science 514 (2020) 145939

Contents lists available at ScienceDirect

Applied Surface Science

journal homepage: www.elsevier.com/locate/apsusc

Full Length Article

Dual remediation of waste waters from methylene blue and chromium (VI) using thermally induced ZnO nanofibers

Mohamed Hilal Elhousseini[a,b,c], Tuğba Isık[d,e], Özlem Kap[f], Francis Verpoort[a,b], Nesrin Horzum[f,*]

[a] State Key Laboratory of Advanced Technology for Materials Synthesis and Processing, Wuhan University of Technology, Wuhan, PR China
[b] School of Materials Science and Engineering, Wuhan University of Technology, Wuhan, PR China
[c] Materials Science and Engineering Department, Izmir Katip Çelebi University, Izmir, Turkey
[d] Materials Science and Engineering Department, Izmir Institute of Technology, Izmir, Turkey
[e] School of Chemistry, University of Bristol, Bristol, United Kingdom
[f] Engineering Sciences Department, Izmir Katip Çelebi University, Izmir, Turkey

ARTICLE INFO

Keywords:
Adsorption
Cooling method
Electrospinning
Photodegradation
Zinc oxide

ABSTRACT

Electrospun zinc oxide (ZnO) nanofibers have been significantly improved via a simple heat treatment modification. The present work reports an intriguing cost-effective microstructure tuning, by drastically dropping the temperature of the calcined sample during the cooling period, to get highly photocatalytically active ZnO nanofibers. The calcination temperatures are deducted from thermogravimetric analysis, the phase and purity are confirmed by X-ray diffraction, while the morphology and texture have been revealed by field emission scanning electron microscopy and high-resolution transmission electron spectroscopy. X-ray photoelectron spectroscopy was conducted to get further insight on the surface composition and oxidation states, while N_2-adsorption isotherms were analyzed using the Brunauer-Emmet-Teller methodology. The crystallinity, surface area, and porosity of the ZnO nanofibers, as well as the exposure of active sites, have been enhanced by the rapid cooling method. Photodegradation activity toward methylene blue was improved from 88% to 94%, and 85% to 97%, for free cooled and rapid cooled samples calcined at 300 °C and 500 °C respectively. The adsorption of chromium (VI) was also tested and reached around 85 mg/g at 100 ppm without being saturated, thereby highlighting one of the most cost-effective performance-enhancing modifications so far that could be extended on different metal oxide nanomaterials.

1. Introduction

The desire to improve the quality of human life has led to fast-growing industrialization and urbanization [1], however, it has come with a heavy cost. Along with air pollution, water pollution is considered as one of the actual significant threats to humanity on earth [2,3]. Among all contaminants in the subject, genotoxic organic and inorganic pollutants such as dyes and heavy metals are putting day-to-day human and animal life at high risk even at low concentrations [4–6]. On top of the scarcity of world water resources, the large worldwide scale production is deeply concerning; around 7×10^5 tons of dye-stuff per year for instance [7]. Therefore, the reuse of wastewaters promptly put breakthroughs in dyes treatment on high demand [8].

To date, various techniques have been deployed for this regard, including chemical oxidation, coagulation, photocatalysis, and adsorption [9]. The latter two remedies are the most widely appreciated due to the cost and energy-related considerations besides the remarkable efficiency and the likeliness of their application on an industrial scale. Many materials such as metal-organic frameworks (MOFs) [10,11], porous organic polymers (POPs) [12,13], etc. have been used for dye degradation and heavy metal adsorption. In spite of the large surface area and hierarchical porous 3D structure, in particular, it is challenging to form organic materials in a wide range of stable and reproducible nanostructures [10,14,15], as well as the inorganic substances. Metal oxides, for instance, possess decent stability and can be synthesized relatively simple and cost-effective at the nanoscale, granting higher surface area together with captivating semiconductor properties [16–18]. Therefore, from the time when Fujishima and Honda have inspected TiO_2 features, numerous achievements have been met, exploiting such inorganic materials as ZnO, MgO, SnO_2, CdS, etc. [19–21]. Moreover, in order to improve the inherent efficiency, different nanostructures have been synthesized during the last decades, and various doping approaches have been employed [20–22], seeking

* Corresponding author at: Engineering Sciences Department, Izmir Katip Çelebi University, 35620 Izmir, Turkey.
E-mail address: nesrin.horzum.polat@ikcu.edu.tr (N. Horzum).

https://doi.org/10.1016/j.apsusc.2020.145939
Received 29 November 2019; Received in revised form 19 February 2020; Accepted 27 February 2020
Available online 28 February 2020
0169-4332/

wider band gaps for better photocatalytic activity. Nevertheless, not many studies have drawn care to bring straightforward changes to the conventional procedures themselves.

ZnO and TiO_2 are found to be the most commonly used among a wide range of binary and ternary metal oxides due to their interesting intrinsic properties, namely the high photosensitivity, wide bandgap, and porous structure [23–25]. Even though TiO_2 has been slightly more attractive and extensively studied for these matters, ZnO remains definitely an excellent candidate; it is more abundant at a lower cost, nontoxic, and eco-friendly, thus shedding more light on the likeliness of its usage. Furthermore, the photocatalytic efficiency of ZnO materials is highly comparable or even better than TiO_2, CeO_2, MgO, SnO_2, etc. [19,22]. Besides that, ZnO may come in different nanoshapes as it is relatively easier to synthesize 0, 1, 2, and 3-dimensional nanostructures out of it [26].

This work addresses ZnO nanofiber fabricated by electrospinning as one of the most effective techniques allowing the utilization of maximum length, stability, and high surface area of the nanofibers, in addition to the facts that the method is simple, cost-effective, and convenient [27,28]. Electrospun ZnO nanofibers are generally long chains of interconnected polycrystalline nanoparticles, providing a high surface to volume ratio, and offering a remarkably large contact surface [27]. Once the nanofiber is illuminated by larger energy than its bandgap, photogenerated electrons migrate to the surface and stimulate the adsorption of oxidative O_2 via the reaction $O_{2(g)} + e^- \rightarrow O_{2(ad)}$. This layer is known to make ZnO nanofibers extremely sensitive to UV light [29].

Relying on our previous work on nanowires [30], we have been interested in the effects of the cooling route after calcination and tried to extend it to the ZnO nanofibers as well, since the latter presents a stretched morphology and a higher surface area, while an enhanced surface area is directly linked to smaller crystallites [30]. In this regard, it has been demonstrated that the rapid cooling method shrinks and thus multiplies the grains. Since the grain boundaries work as traps to holes and hinder the recombination of electron-hole pairs, the conductivity of the material can be improved [16,29]. The different cooling routes for the synthesis of ZnO nanofibers and the effect of the resulting morphology on the photocatalytic activity evaluated by MB degradation and the adsorption efficiency exemplified by Cr(VI) removal is discussed.

2. Materials and methods

2.1. The procedure for fabrication of nanofibers

The mixture of 2.5 g of in a solution of 18 wt% of PVA (4.0 g, Sigma-Aldrich, 87%-90% hydrolyzed, Mw = 30,000–70,000 g/mol) was stirred at 60 °C with 1000 rpm for 5 h, the homogeneous solution of PVA/ZnAc was loaded afterwards into the plastic syringe. The electrospinning experiments were carried out with a home-made electrospinning setup including a pump model (New Era Pump Systems, Inc. NE-300) and a high voltage power supply (Gamma High Voltage Research, Ormond Beach, FL32174). Parameters used on this setup were such as 6 cm for the tip-to-collector distance, while the feed rate was kept constant at 2.5 mL/h and 10 kV potential was applied to the tip of the syringe needle. As-spun PVA/ZnAc nanofibers were collected from the aluminium foil into an alumina crucible placed in a muffle oven (Protherm furnaces, PLF/20/27, Turkey) and calcined at 300, 500, and 700 °C for 6 h with a rate of 2 °C min^{-1}. The resulting nanofibers were named FC-NF@300, FC-NF@500, and FC-NF@700 submitted to free-cooling inside the muffle until reaching room temperature. While RC-NF@300, RC-NF@500, and RC-NF@700 were subjected to a rapid cooling by picking the sample up from the oven right after 6 h period of heating and applying cold water to cool down the edges of alumina crucible.

2.2. Characterization methods

The morphology and texture were studied by scanning electron microscopy (SEM, Carl Zeiss 300VP, Germany) equipped with energy dispersive X-ray spectroscopy (EDX) system and transmission electron microscopy (FETEM - JEM-2100F, Jeol). ZnO nanofibers micrographs were treated via processing software, Fiji ImageJ, to get approximative diameters. A gold coating was applied to the samples using a Q150 RES coater to enhance the conductivity before SEM imaging. SEM micrographs were taken with accelerating voltage of 3.0–10 kV and working distance of 7.0–12.0 mm. The purity and crystallinity of the ZnO nanofibers were investigated via a Philips X' Pert Pro X-Ray diffractometer in theta-theta configuration with a time per step of 15.24 s. A couple tension/current of 45 kV/40 mA was applied on the copper anode, and the diffraction was collected from 5° to 100°. Thermogravimetric analysis (TGA) was performed using a TA Instruments (SDT Q600 V20.9 Build 20) in a range of 20 to 800 °C with a ramp of 10 °C/min. The surface composition of the nanofibers before and after chromium sorption was analyzed by X-ray Photoelectron Spectroscopy (XPS – Thermo Fisher EscaLab 250Xi) with an Al Kα X-rays source. The simulated peaks used for XPS deconvolution were 100% Gaussian type. The XPS database was used (Xpssimplified) for the binding energies values. N_2 adsorption-desorption isotherms were obtained at 77 K via the Brunauer-Emmet-Teller methodology (Micrometrics 3Flex). Fourier transform infrared (FTIR) and the attenuated total reflection (ATR) of the fibers were performed with a spectral resolution of 4 cm^{-1} in a Thermo Scientific Nicolet iS5 spectrometer.

2.3. Photocatalytic performance of ZnO nanofibers

A model reaction was employed for the determination of the photocatalytic activity of ZnO nanofibers. The samples were treated with Methylene Blue (MB) solution under UV irradiation. MB (AppliChem) solution was prepared at a concentration of 0.02 mM at neutral pH. Afterwards, 2.5 mg of each catalyst (FC-NF@500 and RC-NF@500) was added in 25 mL of MB solution and stirred for 20 min in the dark to provide the adsorption and desorption equilibrium between photocatalyst and dye solution. Also, 25 mL of MB solution was prepared without adding any catalyst to control the model reaction. Then, the MB solutions were irradiated with 300 W UV lamp (Osram Ultra Vitalux, German) through 210 min with a distance of 10 cm above the beaker. The degradation percentage of MB solutions was determined by using a UV-Vis spectrophotometer (SHIMADZU, UV 2550, Japan) by observing the color disappearance of MB solution. The percent degradation was calculated by the following equation that A_0 and A_t refers to the initial and final absorbance of MB solutions.

$$\text{Degradation } (\%) = \left(\frac{(A_0 - A_t)}{A_0}\right) \times 100$$

2.4. Photoelectrochemical measurements

Linear sweep voltammetry (LSV) and EIS Nyquist plots were conducted on the electrochemical workstation (CHI 760D, CH Instruments, Inc., Shanghai, China). Ag/AgCl electrode was used as a reference electrode and a platinum electrode as a counter electrode, the working electrode is a glassy carbon with a disk area of 0.07 cm^2, all together submerged in a 1 M KOH solution.

2.5. Chromium adsorption

Visual MINTEQ software was used for the speciation analysis of chromium-containing ions at various pH values (Fig. S1). Batch adsorption studies were conducted to calculate the chromium ion adsorption capacity of ZnO nanofibers. The 1000 ppm chromium solution

was prepared by dissolving potassium chromate (K_2CrO_4, Merck, 99.5%) in ultrapure water. The pH of the solution was adjusted to 2.0 by using hydrochloric acid (HCl, Sigma-Aldrich, 37%) and ammonia (NH_3, Sigma-Aldrich, 28–30%) solutions. Four different concentrations of K_2CrO_4 solutions (5, 10, 50, and 100 ppm) were prepared by the diluting stock solution. The working conditions were set as 120 min for agitation time, 50 °C for reaction temperature and 2.0 for solution pH. These conditions were chosen according to the literature studies for the optimum conditions of Cr(VI) adsorption on ZnO nanostructures [31,32]. The amount of ZnO nanofiber adsorbents was 1 g L^{-1} and the samples were treated with Cr (VI) solutions for 120 min under continuous stirring on a magnetic stirrer. Then, the nanofibers were removed from the solutions and the concentrations of solutions were determined by using the inductively coupled plasma – mass spectrometer (ICP-MS) (Agilent 7500ce Series, Japan). The ICP-MS operation parameters are given in Table S1. The main stock solutions (10, 1.0, 0.10 and 0.010 ppm) were prepared by dilution of 1000 ppm Cr (VI) stock solution. Then, standard solutions of 0.05, 0.1, 0.2, 0.5, 1.0, 2.0, 5.0, 10.0, 20.0, 50.0, 100.0, 200.0, 500.0, 750.0, 1000 and 2000.0 ppb concentrations were prepared by appropriate dilution of main stock solutions to the required volume. Germanium internal standard solution was added in all samples and standard solutions at the same concentration level through all ICP-MS analyses to improve the precision of quantitative analysis. Moreover, all samples and standard solutions were acidified by addition of concentrated HNO_3 to produce 1.0% (v/v) acid in the final solution. For the interpretation of ICP-MS results, a calibration graph is constructed, and the concentration of Cr ions was calculated by using this graph (Fig. S2). The chromium adsorption capacity ZnO nanofibers were calculated from the following equation:

$$Q = \frac{(C_i - C_f)V}{w}$$

where Q is the adsorption capacity (mg g^{-1}) of ZnO nanofibers, C_i is the initial concentration, and C_f is the final concentration of Cr (VI) solutions, V is the volume of solution passed through the adsorbent and w is the weight of adsorbent.

3. Results and discussion

3.1. Structural and morphological analysis of ZnO nanofibers

In order to confirm the effective calcination temperatures, thermal gravimetric analysis (TGA) has been applied on zinc acetate (ZnAc), poly (vinyl alcohol) (PVA) powders, and PVA/ZnAc composite nanofibers (Fig. S3). PVA underwent two stages of weight loss, namely 70% from 268 °C to 350 °C due to the elimination of hydroxyl groups, leaving a residue of conjugated structures and carbonyl groups [33], followed by 13% loss of the final degradation of the organic compounds from 416 °C to 470 °C.

The composite nanofibers displays four losses; water evaporation around 115° (10%), then the decomposition of zinc acetate and PVA organic compounds over three stages of 28%, 9%, 12% occurring respectively at 273 °C, 362 °C and 480 °C, these results come in accordance with previously reported work [34].

X-ray diffraction (XRD) patterns in Fig. 1a and b confirm that increasing the calcination temperature improved the structural crystallinity [30]. More importantly, it clearly reveals the surprising impact that rapid cooling has on the crystallinity and the facet growth. Although 300 °C is shown to be not enough to oxidize nanofibers (Fig. 1a), keeping the same temperature of treatment and subsequently rapid cooling has interestingly improved the crystallinity of the nanofibers by promoting the growth of the main facets (1 0 0) (0 0 2) and (1 0 1) for a wurtzite ZnO (Fig. 1b). Moreover, the 500 °C RC and 700 °C RC samples have noticeably more intense main reflections, that is to say, better crystal quality comparing to adjacent free cooled nanofibers, which returns to the exposition of very hot samples to air enhancing interfacial oxidation process. It is to note that all composite nanofibers treated at 500 and 700 °C, have reflections matching the ZnO wurtzite crystalline phase (reference code: 03–065-3411). No other assignable Bragg peaks have been identified, refuting any alternation of the samples during the process and asserting the purity of the structures.

On the other hand, average crystallite sizes have been estimated by Scherrer equation (see appendix) and listed in Table 1, where ZnO nanofibers show direct proportionality of the crystallite size with rising oxidation temperature due to the deterioration of grain boundaries and thus promoting the merging of the crystallites. Additionally, it is worthy to mention that the 500 °C treated nanofibers have shown a significant dissimilarity. RC-NF@500 displays around 33% larger crystallite size than FC-NF@500, which is consistent to the values of Williamson-Hall (W-H) plots intercepts (Fig. S4), suggesting that the grain boundaries might carry on deteriorating during the cooling period. W-H plot also gave insights about RC-NF@500 and FC-NF@500 XRD peaks broadenings revealing important microstructural strains contribution due to rapid cooling. The lattice parameters are expectedly not changing despite the difference of cooling rate (a = b = 3.24 nm and c = 5.2 nm.).

Fig. 1c and d display the Fourier-transform infrared (FTIR) spectra of the as-prepared and calcined samples that portray relatively the same transmission bands, the intense peaks around 510 cm^{-1} are reflecting the surface phonon modes of Zn—O bond [35]. The single bond from 3000 to 3600 cm^{-1} may be attributed to the return to the stretch modes of O—H, it might also hint on the water molecules that have been absorbed during the test [35–37]. The absorption bands at 1550, 1400 cm^{-1} in the fingerprint region might be ascribed to the symmetric and asymmetric vibrations of the C—O group of PVA, respectively [37]. FTIR showed that the rapid cooling process promotes the presence of the non-volatile carbonyl groups issued from the PVA thermal decomposition, in a clearly higher amount compared with the free cooling process.

Fig. 2a shows the temperature effect on the average diameter on the composite fibers. The smooth texture of non-woven PVA/ZnAc composite nanofibers, with an average size of around 400 nm, is demonstrated in Fig. 2b. The as-prepared ZnO nanofibers in Fig. 2c–h illustrate the effect of raising the calcination temperature from top to bottom, and the cooling method from left to right, free cooling and rapid cooling respectively. A decreasing diameter trend of the calcined ZnO nanofibers is observed. More importantly, the free cooled samples annealed at 500 °C have shortened in diameter in comparison to 300 °C, which is due to the loss of organic matter, leading to the appearance of nanoparticles on what used to be the nanofibers. However, at 700 °C, the shape of the nanofibers is mostly lost and the nanoparticles grow by fusing together due to the high temperature. It is also worth mentioning that the morphology has been considerably affected by the cooling method; rapid cooling has resulted in significant shrinkage in the width for RC-NF@300. Whereas RC-NF@500 has grown relatively larger nanoparticles than FC-NF@500, yielding a noticeably increased width even though the significant loss of carbon related to rapid cooling (Fig. S5). As for 700 °C, RC has also promoted the formation of larger nanoparticles as well as the reduction of carbon content in comparison to FC, nevertheless, both cooling methods resulted in a loss of the fibrous morphology.

Field emission high-resolution transmission electron microscopy (HR-TEM) was performed to examine the textural properties of FC-NF@500 and RC-NF@500. Fig. 3a–f show fibers of width around 154 nm and 177 nm for FC and RC respectively, while these fibers consist out of nanoparticles with a diameter of around 25 nm and 28 nm for FC and RC respectively. These results are consistent with the SEM and XRD results. RC increases the size of the nanoparticles and therefore the width of the whole nanofiber. HR-TEM gives an insight on the (1 0 1) plane of ZnO for both cooling methods, while selected area electron diffraction (SAED) indicates the improvement of the crystallinity due to the rapid cooling modification besides exhibiting a clear hexagonal symmetry returning to the wurtzite structure.

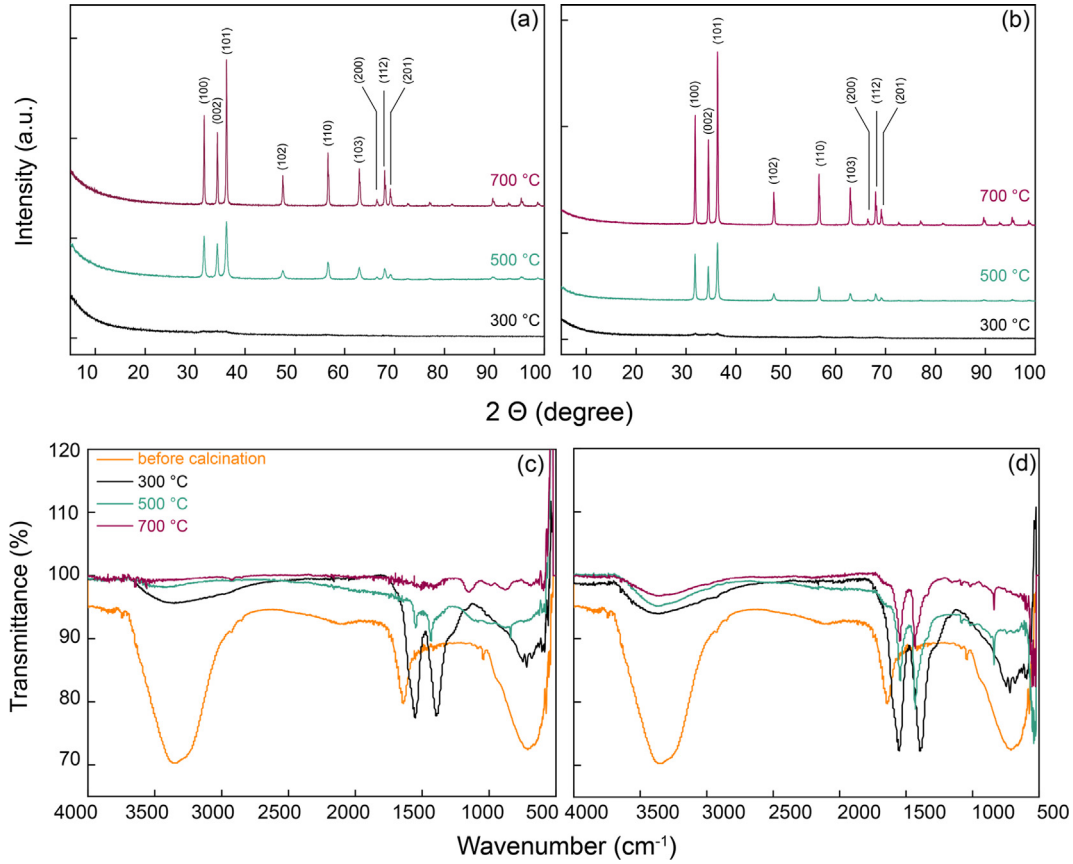

Fig. 1. Structural analysis of free and rapid cooled samples. XRD patterns of (a) the free cooled ZnO NFs, (b) the rapid cooled ZnO NFs. FTIR spectra of (c) free cooled and (d) rapid cooled ZnO NFs.

Table 1
Average crystallite size of the ZnO nanofibers calcined at given temperatures.

Calcination temperature (°C)	Average crystallite size of free cooled ZnO (nm)	Average crystallite size of rapid cooled ZnO (nm)
300	–	–
500	21	28
700	41	40

N_2-adsorption was conducted to investigate the specific surface area of the 500 °C calcined nanofibers, revealing an improved BET surface area, from 7.55 to 10.79 m^2/g, as well as increased pore size, from 17.2 nm to 23.5 nm for free cooling and rapid cooling, respectively. Fig. 3g shows an isotherm type II for both samples with a first inflection point around $P/P_0 = 0.2$, hinting at the formation of the first monolayer. Subsequently, a counter-adsorption takes place and reaches its maximum at a relative pressure of 0.8, followed by capillary condensation. Rapid cooling seems to remarkably enhance the porous structure and significantly improve the maximal adsorption volume from 21 cm^3/g to 41 cm^3/g, for FC-NF@500 and RC-NF@500, respectively. The inset of Fig. 3g shows the pore volume versus pore width plot of the nanofibers, indicating different pore construction of FC-NF@500 and RC-NF@500.

3.2. Photocatalytic performance of ZnO nanofibers

The fabricated ZnO nanofibers were applied as photocatalyst and their degradation performances were tested towards methylene blue (MB). Fig. 4 shows the representative UV–Vis spectra of a 0.02 mM aqueous MB solution in the presence of the RC-NF@500 nanofibers under exposure of 300 W UV light from 0 to 210 min. The increase in irradiation time diminishes the absorption peak corresponding to MB at 663 nm gradually. Long-term UV irradiation of MB (≈210 min) in the presence of RC-NF@500 nanofibers results in up to 97% degradation of MB, and the color of the MB solution has disappeared, as seen in inset figure. Because of the unique electronic configuration and electron-hole pair production abilities of semiconductor metal oxides, they have been taking part in light-catalyzed redox reactions for the last years. Hoffmann et al. proposed, that when the energy of photon matches or exceeds the bandgap energy of the semiconductor, an electron is promoted from the valence band to the conduction band by leaving a hole behind. Then, the excited state electrons in the conduction band and the holes in the valence band can recombine by dissipating energy as heat [38]. ZnO nanostructures have a bandgap of nearly 3.2 eV, which means the photocatalysis reaction can be initiated by applying energy larger than 3.2 eV. The photo-generated electron-hole pair on the surface of the ZnO nanostructures can react with O_2, H_2O or other organic compounds that result in the generation of reactive oxygen species (ROS) in a reaction medium. These ROS could be hydroxyl ($^{\cdot}OH$) or superoxide ($^{\cdot}O_2^-$) radicals as well as hydrogen peroxide (H_2O_2) molecules, and they effectively take part in the oxidation processes of organic pollutants such as MB [39,40].

Photocatalytic degradation of MB solution in the absence of ZnO nanofibers was also demonstrated by placing the dye solution under UV light for 210 min. Only a 23% reduction was observed in the absorbance of MB solution (Fig. S6) which indicates that both UV irradiation and a ZnO catalyst are required together for fast and complete degradation of MB. Fig. 5 represents the percent degradation of MB under UV irradiation in the presence of ZnO nanofibers as a function of time. The percentage of degradation was calculated by using the time-dependent UV-Vis spectra of MB solutions (Fig. S6). The degradation of an MB solution occurs rapidly when FC-NF@500 nanofibers were used as

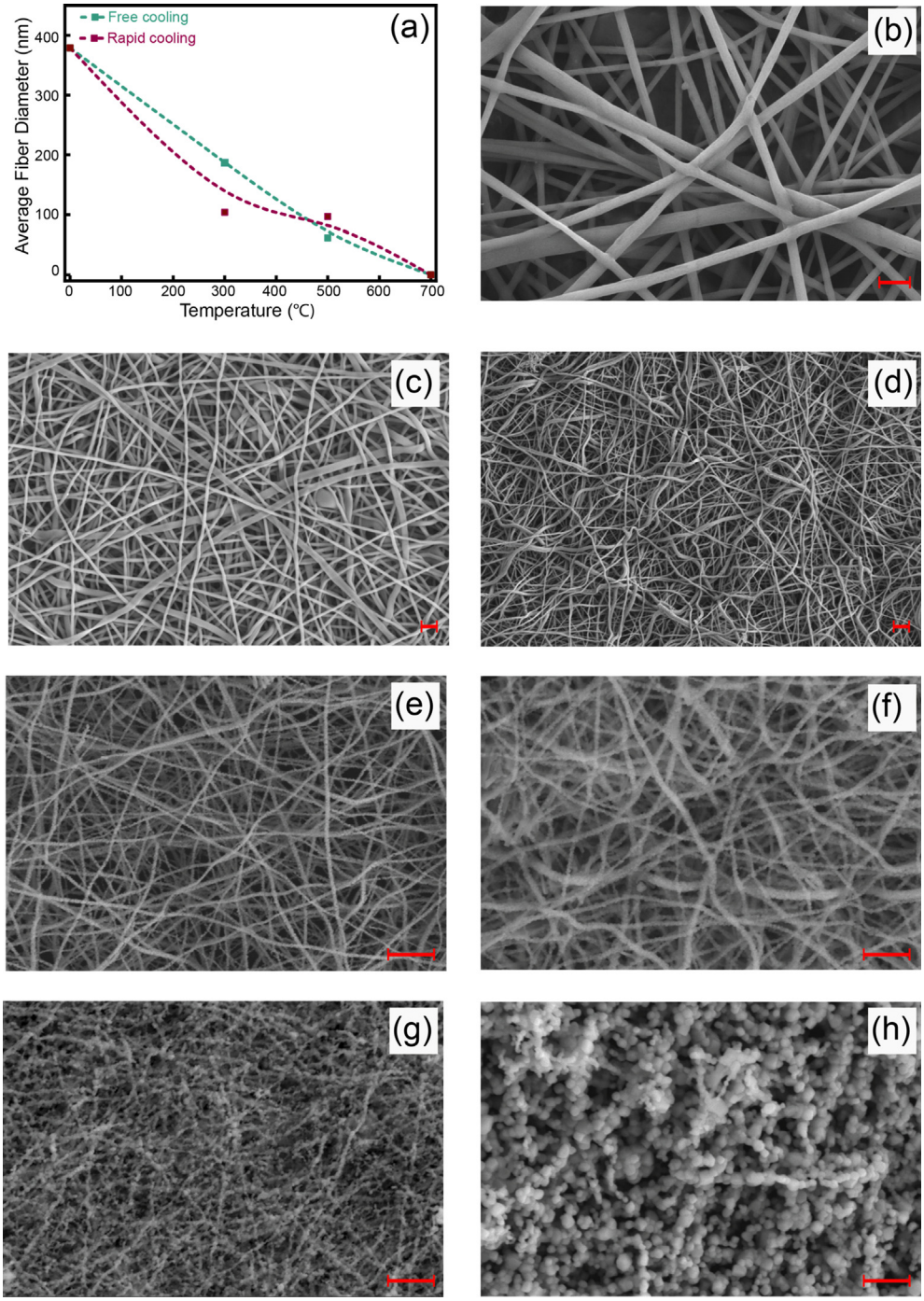

Fig. 2. (a) The variation of average fiber diameter of composite nanofibers before and after calcination. SEM micrographs of PVA/ZnAc composite nanofibers (b) before calcination and after calcination at (c) FC-NF@300, (d) RC-NF@300, (e) FC-NF@500, (f) RC-NF@500, (g) FC-NF@700, and (h) RC-NF@700. Scale bar denotes 1 μm for each micrograph.

photocatalyst and reach 79% at 150 min, while at that time the percent degradation of RC-NF@500 nanofibers was only 70%. However, the percent degradation of rapidly cooled nanofibers (RC-NF@500) overtakes FC-NF@500 ones after that and reaches 97% at 210 min while free cooling reaches only 85% efficiency. The higher degradation rate of FC-NF@500 nanofibers could be the result of their larger average fiber diameter (AFD) and their better dispersion in water. However, the larger the AFD, the smaller the BET surface area, and therefore the FC-NF@500 nanofibers have lower photocatalytic performance than RC-NF@500. The increase in BET surface area of the catalysts results in better photocatalytic performance because of the larger number of active sites on the photocatalytic surfaces [41]. The larger surface area of the RC-NF@500 nanofibers makes the access and participation of the carriers on the photocatalytic surface more available.

Generally, ZnO exhibits weak electrochemical water oxidation on the surface of the electrode with almost no significant photocurrent under visible light [5]. However, the rapid cooling modification has improved noticeably the photoconversion yielding a higher maximum photocurrent at a potential of 0.8 mV (Fig. 6a). The higher photocurrent is related to a strong ability to keep the pairs e^{-}-h^{+} separated longer [42], as well as it returns to an improved rate of photo-induced carriers in the material [43,44]. These results come in accordance with Nyquist

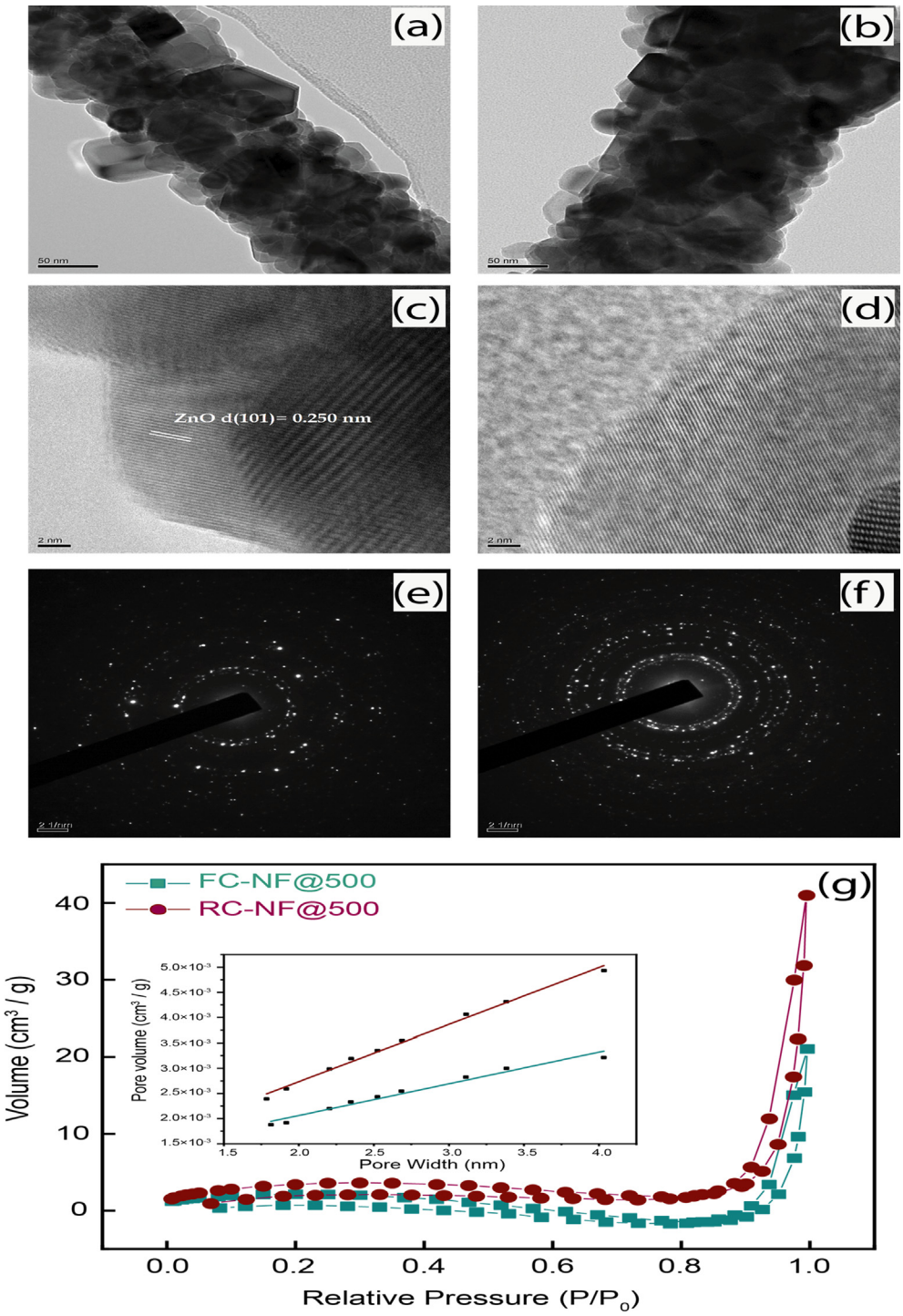

Fig. 3. HR-TEM and SAED of (a, c, e) free cooling and (b, d, f) rapid cooling composite nanofibers calcined at 500 °C. (g) Nitrogen adsorption isotherms of free cooling and rapid cooling composite nanofibers. Inset shows the pore volume versus pore width plot of the nanofibers.

plots (Fig. 6b), RC-NF@500 shows a lower resistance to the interfacial charge transfer than FC-NF@500.

3.3. Cr (VI) adsorption performance of ZnO nanofibers

The adsorbed amount of Cr (VI) ions after 120 min, at a fixed pH of 2.0 at a temperature of 50 °C, was calculated in the presence of 1 g L^{-1} ZnO adsorbent. The pH of the solution system is one of the most significant factors that affect the adsorption performance. It is widely known that the maximum Cr (VI) adsorption can be achieved when highly acidic conditions were maintained in the solution [31,32,45]. The dominant species of Cr (VI) in aqueous solutions are CrO_4^{-2} (chromate) and $HCrO_4^-$ (hydrogen chromate) (Fig. S1b). While at highly acidic conditions, meaning low pH, a majority of CrO_4^{-2} species are found, at basic conditions $HCrO_4^-$ species are stable. ZnO nanoparticles show a tendency to adsorb $HCrO_4^-$ species while at high pH values, Cr (VI) ion removal is inhibited due to the competition with the OH^- ions in the solution [45]. Thus, the working pH for the adsorption trials was set to 2.0 through this study. The adsorbed amount of analyte species increases with an increase in adsorbent dose because of the

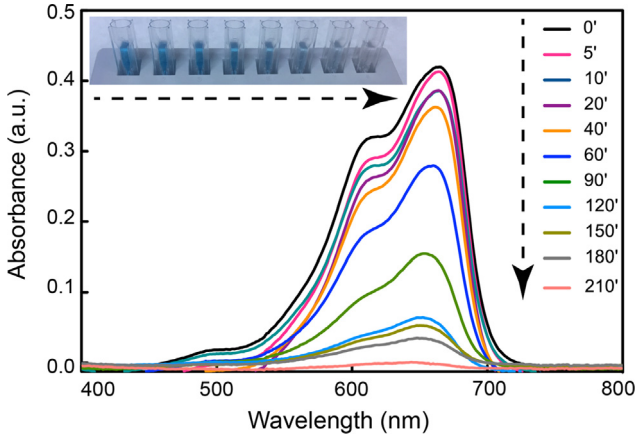

Fig. 4. UV-Visible spectra of MB solutions under UV light irradiation in the presence of RC-NF@500 nanofibers. Inset: Color change of MB solution over 210 min.

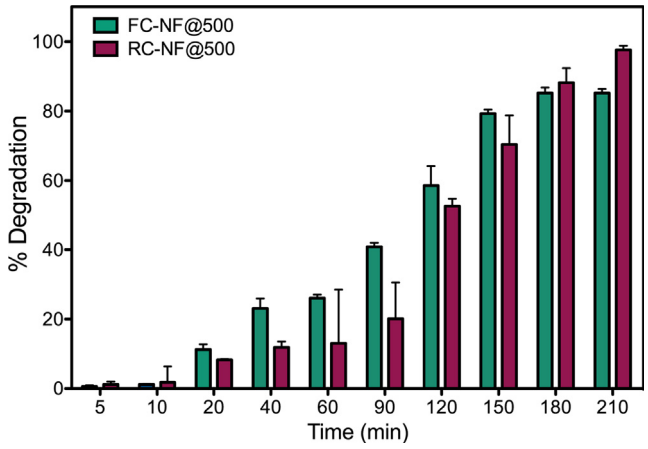

Fig. 5. Percentage degradation of MB solution under UV radiation as a function of time using FC-NF@500 and RC-NF@500 nanofibers (2.5 mg nanofiber in 25 mL of 0.02 mM MB solution).

presence of a larger number of active sites and after a certain point equilibrium is achieved [46]. Khan et al. and Olivera et al. showed that equilibrium was attained when 1 g L^{-1} ZnO adsorbent was used for the removal Cr (VI) ions [45,46]. According to this information, we decided to use an adsorbent dosage of 1 g L^{-1} (ZnO nanofibers). The adsorption of Cr (VI) ions is an endothermic process as the species need enough

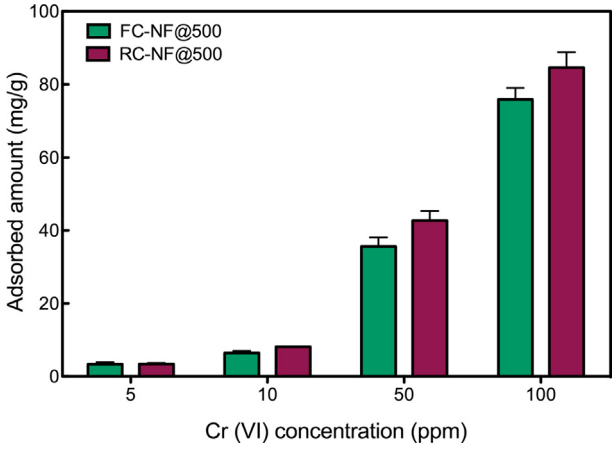

Fig. 7. Chromium adsorption capacity of FC and RC ZnO nanofibers as a function of initial concentration (pH ≈ 2.0, adsorbent dosage = 1 g L^{-1}, temperature = 120 °C, contact time = 120 min).

energy to interact with the active sites of the adsorbent. This is because the diffusion and mobility of the analyte species increase at higher temperatures. Therefore the temperature for the adsorption process was set as 50 °C [47,48]. In the literature, various contact times have been tried in order to achieve maximum Cr (VI) adsorption [31,32,45,49]. The required contact time was chosen as 120 min during the adsorption process to obtain the highest adsorption. The adsorption of Cr (VI) ions was carried out at four different initial chromium ion concentrations, ranging from 5 to 100 ppm (Fig. 7).

When the initial Cr (VI) concentration increased from 5 to 100 ppm, the adsorbed Cr (VI) amount increased from 3.3 ± 0.6 to 75.9 ± 3.2 mg/g and 3.4 ± 0.4 to 84.6 ± 4.2 mg/g for FC-NF@500 and RC-NF@500, respectively. The uptake of Cr (VI) ions at high initial concentration increases because a high concentration provides a driving force to overcome the mass transfer resistances of the pollutant between the aqueous and solid phases [50,51]. The adsorption capacity of the fibers does not reach any saturation, even at 100 ppm Cr (VI) concentration, because of their high surface area. Table 2 shows a comparison of the maximum adsorption capacities of various adsorbents for the removal of Cr (VI) ions from aqueous solutions. The relatively higher adsorption capacity of ZnO nanofibers makes them a suitable adsorbent for the removal of hexavalent chromium ions from aqueous solutions. Moreover, this study is the first in literature that utilizes ZnO nanofibers in Cr (VI) adsorption.

For further elemental interpretations, XPS analysis was performed for FC500 and RC500 nanofibers before and after Cr (VI) adsorption.

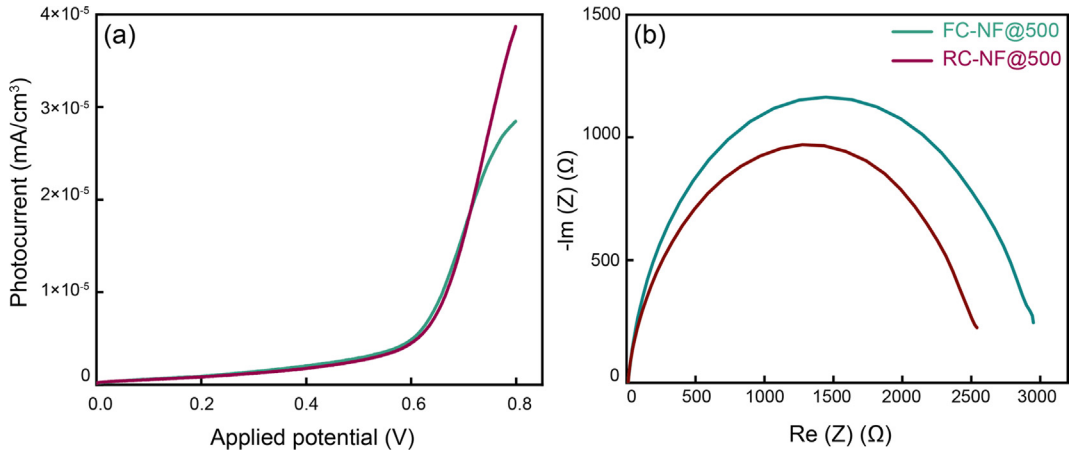

Fig. 6. Linear sweep voltammetry (LSV) spectra performed at a scan rate of 50 mV in 1 M KOH solution (a), and Nyquist plots (b) of FC-NF@500 and RC-NF@500.

Table 2
Comparison of different adsorbents for Cr (VI) uptake in the literature.

Adsorbent	Adsorbent dose (g/L)	Contact time (min)	pH	Adsorption capacity (mg/g)	Ref
Guar gum–nano zinc oxide (GG/nZnO) biocomposite	1.0	50	7.0	55.56	[46]
Nano ZnO nanoparticles	4.0	90	2.0	26.7	[32]
Iron containing Activated carbon	0.6	2880	5.0	68.49	[52]
Activated carbon from *Hevea Brasilinesis* sawdust	1.0	300	2.0	44.05	[53]
$NiFe_2O_4$ doped hollow fiber mixed membrane	0.15	1440	7.0	18.0	[54]
Tea factory waste	10.0	60	2.0	54.65	[47]
ZnO nanofibers	1.0	120	2.0	84.6	This study

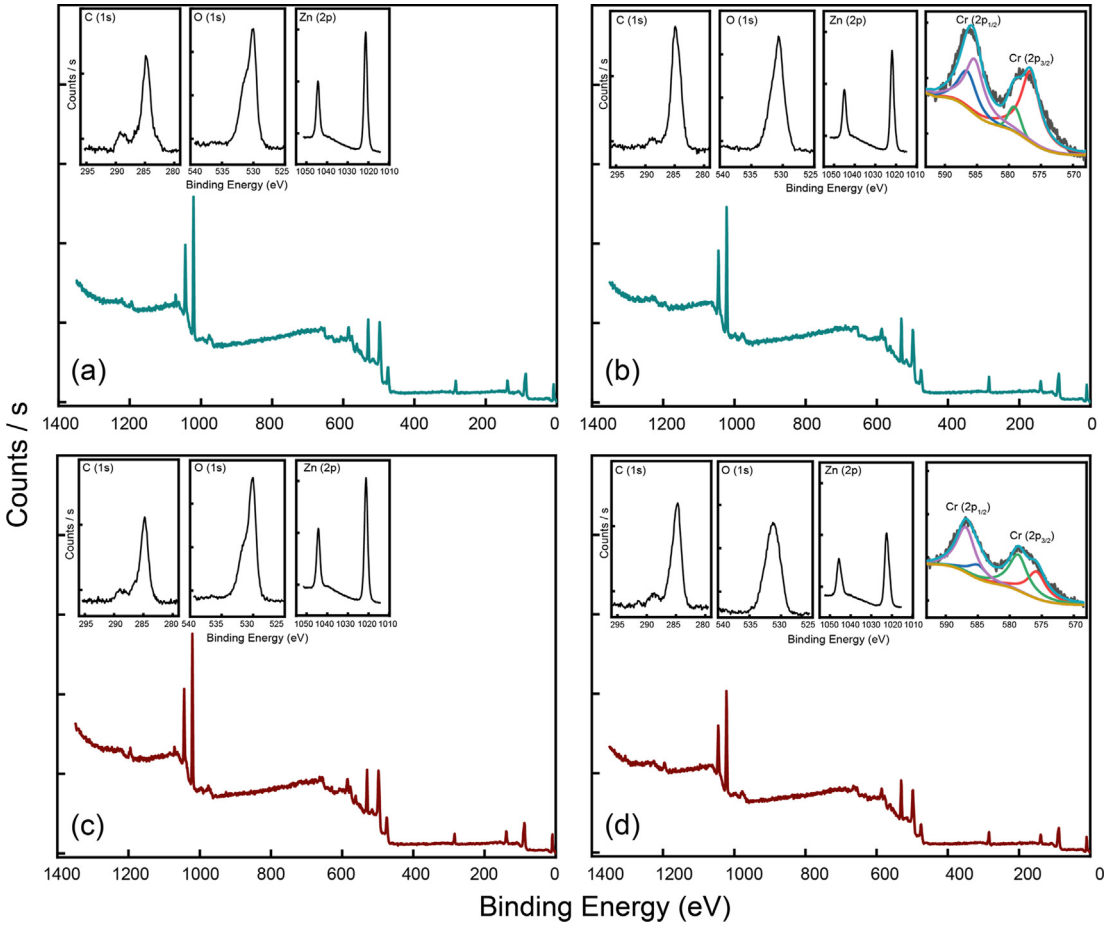

Fig. 8. XPS spectra of (a-b) FC-NF@500 and (c-d) RC-NF@500 nanofibers for before and after Cr(VI) sorption, respectively. The insets show the spectra of C (1 s), O (1 s), Zn (2p), Cr ($2p_{1/2}$) and Cr($2p_{2/3}$) orbitals.

Firstly, the adsorbents were analyzed with XPS and the photoemission bands C(1s), O(1s) and Zn(2p) were recorded in order to characterize their functional groups before Cr (VI) adsorption (Fig. 8a and c). The C(1s) spectra of FC-NF@500 and RC-NF@500 appears around 284 and 288 eV, assigned to the C—C and C—O bonds [55] (insets in Fig. 8). The O(1s) spectra of the samples were obtained and a peak around 531 eV was found, which could be ascribed to the presence of hydroxides [56], Zn($2p_{3/2}$) and Zn($2p_{1/2}$) were observed in the survey XPS spectra of all samples at 1021 and 1044 eV, respectively. These spectra of Zn(2p) are simple spin-orbit doublets generally corresponding to the ZnO wurtzite structure [57,58]. (Figs. S7 and S8)

For the clarification of the adsorption mechanism for Cr(VI) on FC-NF@500 and RC-NF@500 nanofibers, the XPS spectra are plotted in Fig. 8b and d after adsorption. Two energy bands at around 577 and 588 eV correspond to the binding energies of Cr ($2p_{3/2}$) and Cr ($2p_{1/2}$), respectively. The presence of these two bands confirms the existence of both Cr(III) and Cr(VI) on the surface of the fibers. The Cr(III) peak suggests that some Cr(VI) adsorbed on the surface of ZnO nanofibers is reduced to Cr(III) [55,59]. (Fig. S9)

The proposed mechanisms for metal ion removal from aqueous systems can be classified as (i) oxidation/reduction by photogeneration of electron-hole pairs and (ii) physical adsorption. The photoreduction of chromium ions on the ZnO surface contributes to the heavy metal ion removal in aqueous systems [60]. At the acidic conditions, the nanofiber surface is protonated and positively charged (Fig. S1a). Thus, the positively charged adsorption sites can attract the negatively charged anionic forms of the Cr (VI) species [32] (Fig. S1b).

The atomic percentages of carbon, oxygen, zinc and chromium species on the surface of the adsorbents are summarized in Table 3. The atomic percentages of carbon and oxygen are nearly the same for all samples before and after adsorption. Moreover, the atomic percentage of zinc species decreases for both samples after chromium adsorption as the adsorbed Cr ions might shield the detection of Zn on the surface of the fibers. There is a further reduction in the atomic percentage of Zn

Table 3
Surface chemical composition of ZnO nanofiber adsorbents before and after adsorption calculated from XPS spectra.

Adsorbent	C(1s) %	O(1s) %	Zn(2p) %	Cr(2p) %	Cr/Zn
FC-NF@500 before	30.83	41.14	28.03	N/A	0
FC-NF@500 after	31.91	37.86	23.04	7.18	0.31
RC-NF@500 before	26.11	42.33	31.56	N/A	0
RC-NF@500 after	31.8	41.06	23.27	3.88	0.17

(2p) for RC-NF@500 nanofibers (26%) compared to the FC-NF@500 ones (18%), which means that there must be more adsorbed chromium ions on the surface of the RC-NF@500. However, both the atomic percentage of Cr(2p) species and the Cr/Zn ratio on FC-NF@500 is nearly two-fold larger than for RC-NF@500. This is in contrast with the ICP-MS results which proved that RC-NF@500 promotes wider adsorption into the bulk through its largely developed porous structure.

4. Conclusions

A simple and efficient strategy was proposed to enhance the photocatalytic degradation performance of metal oxides in addition to their adsorption ability. This study reports the first application of a rapid cooling method after calcination of PVA/ZnAc nanofibers fabricated by electrospinning. The properties and performance of the obtained microstructure after 5 h of constant heating and a subsequent thermal shock were investigated. The results revealed the intriguing improvement of the porous structure, crystalline properties and interfacial oxidation of the fibers. The outcome of the free and rapid cooled ZnO nanofibers was evaluated, and the rapid cooling method exhibited an enhanced methylene blue photodegradation activity from 85% to 97%, as well as an increase in chromium (VI) adsorption in acidic media from 76 to 85 mg/g for FC-NF@500 and RC-NF@500, respectively. This approach could also be of great use for the application of photocatalysis and adsorption in the treatment of wastewaters containing heavy metals and organic pollutants in various textile, printing, and chemical industries.

CRediT authorship contribution statement

Mohamed Elhousseini Hilal: Conceptualization, Investigation, Writing - original draft. **Tuğba Isık:** Investigation, Visualization, Writing - original draft. **Özlem Kap:** Investigation, Writing - review & editing. **Francis Verpoort:** Resources, Writing - review & editing. **Nesrin Horzum:** Methodology, Resources, Supervision, Writing - review & editing.

Acknowledgement

The authors acknowledge to E. Culcular for his assistance with SEM at IKCU Central Research Laboratory and S. E. Kınal from IzTech Environmental Research and Development Center for her assistance in ICP-MS measurements. M.E.H. would like to acknowledge State Key Laboratory of Advanced Technology for Materials Synthesis and Processing, Wuhan University of Technology and Materials Science and Engineering Department, Izmir Katip Çelebi University. M.E.H. expresses his deep appreciation to the Chinese Scholarship Council (CSC) for his Ph.D. study grant (no. 2017GXZ001124).

Appendix

Scherrer equation as published on 1918 $\beta(2\theta) = \frac{K\lambda}{D\cos\theta}$.where $\beta(2\theta)$ the full width at high maximum (FWHM) is inversely proportional to the crystallite size D, K represents a dimensionless shape factor with a value 0.9, λ is X-ray wavelength of Cu and θ is Bragg angle.

Appendix A. Supplementary material

Supplementary data to this article can be found online at https://doi.org/10.1016/j.apsusc.2020.145939.

References

[1] A. Singh, A. Bhati, P. Khare, K.M. Tripathi, S.K. Sonkar, Soluble graphene nanosheets for the sunlight-induced photodegradation of the mixture of dyes and its environmental assessment, Sci. Rep. 9 (2019) 2522, https://doi.org/10.1038/s41598-019-38717-1.
[2] C. Liu, D. Kong, P. Hsu, H. Yuan, H. Lee, Y. Liu, H. Wang, S. Wang, K. Yan, D. Lin, P.A. Maraccini, K.M. Parker, A.B. Boehm, Y. Cui, Rapid water disinfection using vertically aligned MoS_2 nanofilms and visible light, Nat. Nanotechnol. 11 (2016) 1098–1104, https://doi.org/10.1038/nnano.2016.138.
[3] Z.P. Cano, D. Banham, S. Ye, A. Hintennach, J. Lu, M. Fowler, Z. Chen, Batteries and fuel cells for emerging electric vehicle markets, Nat. Energy. 3 (2018) 279–289, https://doi.org/10.1038/s41560-018-0108-1.
[4] A. Arques, A.M. Amat, A. García-Ripoll, R. Vicente, Detoxification and / or increase of the biodegradability of aqueous solutions of dimethoate by means of solar photocatalysis, J. Hazard. Mater. 146 (2007) 447–452, https://doi.org/10.1016/j.jhazmat.2007.04.046.
[5] D. Neena, K.K. Kondamareddy, H. Bin, D. Lu, P. Kumar, R.K. Dwivedi, V.O. Pelenovich, X.-Z. Zhao, W. Gao, D. Fu, Enhanced visible light photodegradation activity of RhB/MB from aqueous solution using nanosized novel Fe-Cd co-modified ZnO, Sci. Rep. 8 10691 (2018), https://doi.org/10.1038/s41598-018-29025-1.
[6] K. He, G. Chen, G. Zeng, A. Chen, Z. Huang, J. Shi, T. Huang, M. Peng, L. Hu, Three-dimensional graphene supported catalysts for organic dyes degradation, Appl. Catal. B. 228 (2018) 19–28, https://doi.org/10.1016/j.apcatb.2018.01.061.
[7] J.G. Huddleston, H.D. Willauer, R.P. Swatloski, A.E. Visser, R.D. Rogers, Room temperature ionic liquids as novel media for 'clean' liquid – liquid extraction, Chem. Commun. 1765–1766 (1998), https://doi.org/10.1039/a803999b.
[8] F. Long, J. Gong, G. Zeng, L. Chen, X. Wang, J. Deng, Q.-Y. Niu, H.-Y. Zhang, X.-R. Zhang, Removal of phosphate from aqueous solution by magnetic Fe – Zr binary oxide, Chem. Eng. J. 171 (2011) 448–455, https://doi.org/10.1016/j.cej.2011.03.102.
[9] V. Kumar, D. Pathania, S. Agarwal, P. Singh, Adsorptional photocatalytic degradation of methylene blue onto pectin – CuS nanocomposite under solar light, J. Hazard. Mater. 243 (2012) 179–186, https://doi.org/10.1016/j.jhazmat.2012.10.018.
[10] J.E. Efome, D. Rana, T. Matsuura, C.Q. Lan, Metal–organic frameworks supported on nanofibers to remove heavy metals, J. Mater. Chem. A. 6 (2018) 4550–4555, https://doi.org/10.1039/C7TA10428F.
[11] Y. Peng, H. Huang, Y. Zhang, C. Kang, S. Chen, L. Song, D. Liu, C. Zhong, A versatile MOF-based trap for heavy metal ion capture and dispersion, Nat. Commun. 9 (2018) 187, https://doi.org/10.1038/s41467-017-02600-2.
[12] M.X. Tan, Y.N. Sum, J.Y. Ying, Y. Zhang, A mesoporous poly-melamine-formaldehyde polymer as a solid sorbent for toxic metal removal, Energy Environ. Sci. 6 (2013) 3254–3259, https://doi.org/10.1039/C3EE42216J.
[13] H. Ou, Q. You, J. Li, G. Liao, H. Xia, D. Wang, A rich-amine porous organic polymer: an efficient and recyclable adsorbent for removal of azo dye and chlorophenol, RSC Adv. 6 (2016) 98487–98497, https://doi.org/10.1039/C6RA18380H.
[14] O. Fleker, A. Borenstein, R. Lavi, L. Benisvy, S. Ruthstein, D. Aurbach, Preparation and properties of metal organic framework / activated carbon composite materials, Langmuir 32 (2016) 4935–4944, https://doi.org/10.1021/acs.langmuir.6b00528.
[15] K. Vikrant, V. Kumar, K.-H. Kim, D. Kukkar, Metal–organic frameworks (MOFs): potential and challenges for capture and abatement of ammonia, J. Mater. Chem. A. 5 (2017) 22877–22896, https://doi.org/10.1039/c7ta07847a.
[16] K.P. McKenna, A.L. Shluger, Electron and hole trapping in polycrystalline metal oxide materials, Proc. R. Soc. A. 467 (2011) 2043–2053, https://doi.org/10.1098/rspa.2010.0518.
[17] Y. Sun, Z. Shen, S. Xin, L. Ma, C. Xiao, S. Ding, F. Li, G. Gao, Ultrafine Co-doped ZnO nanoparticles on reduced graphene oxide as an efficient electrocatalyst for oxygen reduction reaction, Electrochim. Acta. 224 (2017) 561–570, https://doi.org/10.1016/j.electacta.2016.12.021.
[18] P. Sutradhar, M. Debbarma, M. Saha, Microwave synthesis of zinc oxide nanoparticles using coffee powder extract and its application for solar cell, Synth. React. Inorg., Met.-Org. Nano-Met.Chem. 46 (2016) 1622–1627, https://doi.org/10.1080/15533174.2015.1137035.
[19] R. Saravanan, E. Thirumal, V.K. Gupta, V. Narayanan, A. Stephen, The photocatalytic activity of ZnO prepared by simple thermal decomposition method at various temperatures, J. Mol. Liq. 177 (2013) 394–401, https://doi.org/10.1016/j.molliq.2012.10.018.
[20] S. Bera, H. Khan, I. Biswas, S. Jana, Applied surface science polyaniline hybridized surface defective ZnO nanorods with long-term stable photoelectrochemical activity, Appl. Surf. Sci. 383 (2016) 165–176, https://doi.org/10.1016/j.apsusc.2016.05.009.
[21] R. Saravanan, E. Sacari, F. Gracia, M.M. Khan, E. Mosquera, V.K. Gupta, Conducting PANI stimulated ZnO system for visible light photocatalytic degradation of coloured dyes, J. Mol. Liq. 221 (2016) 1029–1033, https://doi.org/10.1016/j.molliq.2016.06.074.
[22] R. Saravanan, N. Karthikeyan, V.K. Gupta, E. Thirumal, P. Thangadurai, ZnO/Ag nanocomposite: An efficient catalyst for degradation studies of textile effluents

under visible light, Mater. Sci. and Eng. C. 33 (2013) 2235–2244, https://doi.org/10.1016/j.msec.2013.01.046.
[23] B. Pant, H.R. Pant, N.A.M. Barakat, M. Park, K. Jeon, Y. Choi, H.Y. Kim, Carbon nanofibers decorated with binary semiconductor (TiO_2/ZnO) nanocomposites for the effective removal of organic pollutants and the enhancement of antibacterial activities, Ceram. Int. 39 (2013) 7029–7035, https://doi.org/10.1016/j.ceramint.2013.02.041.
[24] B. Pant, G.P. Ojha, H.Y. Kim, M. Park, S.J. Park, Fly-ash-incorporated electrospun zinc oxide nanofibers: potential material for environmental remediation, Environ. Pollut. 245 (2019) 163–172, https://doi.org/10.1016/j.envpol.2018.10.122.
[25] B. Pant, M. Park, H.Y. Kim, S.J. Park, Ag-ZnO photocatalyst anchored on carbon nanofibers: Synthesis, characterization, and photocatalytic activities, Synth. Met. 220 (2016) 533–537, https://doi.org/10.1016/j.synthmet.2016.07.027.
[26] T. Isık, M.E. Hilal, N. Horzum, Green synthesis of zinc oxide nanostructures, Zinc Oxide Based Nano Materials and Device, Intechopen, 2018, https://doi.org/10.5772/intechopen.83338.
[27] A. Baranowska-Korczyc, K. Fronc, Ł. Kłopotowski, A. Reszka, K. Sobczak, W. Paszkowicz, K. Dybko, P. Dłuzewski, B.J. Kowalski, D. Elbaum, Light-and environment-sensitive electrospun ZnO nanofibers, RSC Adv. 3 (2013) 5656–5662, https://doi.org/10.1039/c3ra40358k.
[28] B. Al-Ghafri, T. Bora, P. Sathe, S. Dobrestov, M. Al-Abri, Photocatalytic microbial removal and degradation of organic contaminants of water using PES fiber, Appl. Catal. B. 233 (2018) 136–142, https://doi.org/10.1016/j.apcatb.2018.03.095.
[29] G. Shen, D. Chen, One-dimensional nanostructures for photodetectors, Recent Pat. Nanotechnol. 4 (2010) 20–31, https://doi.org/10.2174/187221010790712101.
[30] N. Horzum, M.E. Hilal, T. Isık, Enhanced bactericidal and photocatalytic activities of ZnO nanostructures by changing the cooling route, New J. Chem. 42 (2018) 11831–11838, https://doi.org/10.1039/c8nj01849a.
[31] A. Sharma, K. Kishor, P. Mehta, D. Pathania, Efficient adsorption of chlorphenir-amine and hexavalent chromium (Cr(VI)) from water system using agronomic waste material, Sustain. Chem. Pharm. 9 (2018) 1–11, https://doi.org/10.1016/j.scp.2018.04.002.
[32] N.M. Ahmed, Synthesis and characterization of zinc oxide nano particles for the removal of Cr (VI), Int. J. Sci. Eng. Res. 6 (2015) 1235–1243 https://www.ijser.org/onlineResearchPaperViewer.aspx?Synthesis-and-Characterization-of-Zinc-Oxide-Nano-particles-for-the-removal-of-Cr-VI.pdf.
[33] P. Taylor, H. Yang, S. Xu, L. Jiang, Y. Dan, Thermal decomposition behavior of poly (vinyl alcohol) with different hydroxyl content, J. Macromol. Sci., Part B: Phys. 51 (2013) 464–480, https://doi.org/10.1080/00222348.2011.597687.
[34] M. Imran, S. Haider, K. Ahmad, A. Mahmood, W.A. Al-Masry, Fabrication and characterization of zinc oxide nanofibers for renewable energy applications, Arabian J. Chem. 10 (2017) S1067–S1072, https://doi.org/10.1016/j.arabjc.2013.01.013.
[35] R.M. Alwan, Q.A. Kadhim, K.M. Sahan, R.A. Ali, R.J. Mahdi, N.A. Kassim, A.N. Jassim, Synthesis of zinc oxide nanoparticles via sol – gel route and their characterization, Nanosci. Nanotechnol. 5 (2015) 1–6, https://doi.org/10.5923/j.nn.20150501.01.
[36] Z. Wu, M. Wang, L. Zhou, Z. Yin, J. Tan, J. Zhang, Q. Chen, Framework-solvent interactional mechanism and effect of NMP / DMF on solvothermal synthesis of [Zn4O (BDC)3]8, Trans. Nonferrous Met. Soci. China. 24 (2014) 3722–3731, https://doi.org/10.1016/S1003-6326(14)63521-4.
[37] E. Ghafari, Y. Feng, Y. Liu, I. Ferguson, N. Lu, Investigating process-structure relations of ZnO nano fiber via electrospinning method, Compos. Part B 116 (2017) 40–45, https://doi.org/10.1016/j.compositesb.2017.02.026.
[38] S.R. Dhariwal, L.S. Kothari, S.C. Jain, On the recombination of electrons and holes at traps with finite relaxation time, Solid-State Electron 24 (1981) 749–752, https://doi.org/10.1016/0038-1101(81)90056-3.
[39] Y. Nosaka, A.Y. Nosaka, Generation and detection of reactive oxygen species in photocatalysis, Chem. Rev. 117 (2017) 11302–11336, https://doi.org/10.1021/acs.chemrev.7b00161.
[40] P. Singh, A. Nanda, Synthesis of highly dispersed zinc oxide nanoparticles through ultrasonication assisted by hydrothermal treatment: A novel approach, Synth. React. Inorg. Met.-Org. Nano-Met. Chem. 45 (2015) 1327–1336, https://doi.org/10.1080/15533174.2013.862711.
[41] A. Balcha, O.P. Yadav, T. Dey, Photocatalytic degradation of methylene blue dye by zinc oxide nanoparticles obtained from precipitation and sol-gel methods, Environ. Sci. Pollut. Res. 23 (2016) 25485–25493, https://doi.org/10.1007/s11356-016-7750-6.
[42] R. Saravanan, M.M. Khan, V.K. Gupta, E. Mosquera, F. Gracia, V. Narayanan, A. Stephen, ZnO/Ag/Mn_2O_3 nanocomposite for visible light-induced industrial textile effluent degradation, uric acid and ascorbic acid sensing and antimicrobial activity, RSC Adv. 5 (2015) 34645–34651, https://doi.org/10.1039/C5RA02557E.
[43] S.A. Ansari, J. Lee, M.H. Cho, Biogenic synthesis, photocatalytic, and photoelectrochemical performance of Ag–ZnO nanocomposite, J. Phys. Chem. C. 117 (2013) 27023–27030, https://doi.org/10.1021/jp410063p.
[44] J.J. Beltran, C.A. Barrero, A. Punnoose, Combination of defects plus mixed valence of transition metals : a strong strategy for ferromagnetic enhancement in ZnO nanoparticles, J. Phys. Chem. C. 120 (2016) 8969–8978, https://doi.org/10.1021/acs.jpcc.6b00743.
[45] S. Olivera, C. Hu, G. Shivashankara, A.M. Asiri, The adsorptive removal of Cr (VI) ions and antibacterial activity studies on hydrothermally synthesized iron oxide and zinc oxide nanocomposite, J. Taiwan Inst. Chem. Eng. 93 (2018) 342–349, https://doi.org/10.1016/j.jtice.2018.07.042.
[46] T.A. Khan, M. Nazir, I. Ali, A. Kumar, Removal of Chromium(VI) from aqueous solution using guar gum-nano zinc oxide biocomposite adsorbent, Arabian J. Chem. 10 (2013) S2388–S2398, https://doi.org/10.1016/j.arabjc.2013.08.019.
[47] E. Malkoc, Y. Nuhoglu, Potential of tea factory waste for chromium (VI) removal from aqueous solutions : Thermodynamic and kinetic studies, Sep. Purif. Technol. 54 (2007) 291–298, https://doi.org/10.1016/j.seppur.2006.09.017.
[48] H. Demiral, I. Demiral, F. Tümsek, B. Karabacakoğlu, Adsorption of chromium (VI) from aqueous solution by activated carbon derived from olive bagasse and applicability of different adsorption models, Chem. Eng. J. 144 (2008) 188–196, https://doi.org/10.1016/j.cej.2008.01.020.
[49] M. Dinari, A. Haghighi, Ultrasound-assisted synthesis of nanocomposites based on aromatic polyamide and modified ZnO nanoparticle for removal of toxic Cr(VI) from water, Ultrason. Sonochem. 41 (2018) 75–84, https://doi.org/10.1016/j.ultsonch.2017.09.023.
[50] S. Dawood, T.K. Sen, C. Phan, Synthesis and characterisation of novel-activated carbon from waste biomass pine cone and its application in the removal of congo red dye from aqueous solution by adsorption, Water Air Soil Pollut. 225 (2014) 1818, https://doi.org/10.1007/s11270-013-1818-4.
[51] F. Nekouei, S. Nekouei, I. Tyagi, V.K. Gupta, Kinetic, thermodynamic and isotherm studies for acid blue 129 removal from liquids using copper oxide nanoparticle-modified activated carbon as a novel adsorbent, J. Mol. Liq. 201 (2015) 124–133, https://doi.org/10.1016/j.molliq.2014.09.027.
[52] W. Liu, J. Zhang, C. Zhang, L. Ren, Preparation and evaluation of activated carbon-based iron-containing adsorbents for enhanced Cr(VI) removal : Mechanism study, Chem. Eng. J. 189–190 (2012) 295–302, https://doi.org/10.1016/j.cej.2012.02.082.
[53] T. Karthikeyan, S. Rajgopal, L.R. Miranda, Chromium (VI) adsorption from aqueous solution by Hevea Brasilinesis sawdust activated carbon, J. Hazard. Mater. 124 (2005) 192–199, https://doi.org/10.1016/j.jhazmat.2005.05.003.
[54] M. Mondal, M. Dutta, S. De, A novel ultrafiltration grade nickel iron oxide doped hollow fiber mixed matrix membrane: Spinning, characterization and application in heavy metal removal, Sep. Purif. Technol. 188 (2017) 155–166, https://doi.org/10.1016/j.seppur.2017.07.013.
[55] B. Feng, W. Shen, L. Shi, S. Qu, Adsorption of hexavalent chromium by polyacrylonitrile-based porous carbon from aqueous solution, R. Soc. Open Sci. 5 (2018) 171662, https://doi.org/10.1098/rsos.171662.
[56] V.I. Nefedov, M.N. Firsov, I.S. Shaplygin, Electronic structures of $MRhO_2$, MRh_2O_4, $RhMO_4$ and Rh_2MO_6 on the basis of X-ray spectroscopy and ESCA data, J. Electron Spectrosc. 26 (1982) 65–78, https://doi.org/10.1016/0368-2048/82/87006-0.
[57] A. Ievtushenko, O. Khyzhun, I. Shtepliuk, V. Tkach, V. Lazorenko, G. Lashkarev, X-Ray photoelectron spectroscopy study of nitrogen and aluminum nitrogen doped ZnO Films, Proc. 42th “Jaszowiec” Int. School Conf. Phys. Semiconduct. 18 (2013) 858–862, https://doi.org/10.12693/APhysPolA.124.858.
[58] G. Deroubaix, P. Marcus, X-ray photoelectron spectroscopy analysis of copper and zinc oxides and sulphides, Surf. Interf. Anal. 18 (1992) 39–46, https://doi.org/10.1002/sia.740180107.
[59] C. Bao, M. Chen, X. Jin, D. Hu, Q. Huang, Efficient and stable photocatalytic reduction of aqueous hexavalent chromium ions by polyaniline surface-hybridized ZnO nanosheets, J. Mol. Liq. 279 (2019) 133–145, https://doi.org/10.1016/j.molliq.2019.01.122.
[60] A.T. Le, S.-Y. Pung, S. Sreekantan, A. Matsuda, D.P. Huynh, Mechanisms of removal of heavy metal ions by ZnO particles, Heliyon. 5 (2019) e01440, https://doi.org/10.1016/j.heliyon.2019.e01440.